W-Band Photonic Pulse Compression Radar With Dual Transmission Mode Beamforming

Bohao Liu, Suparna Seshadri (ID), Jhih-Min Wun, Nathan P. O'Malley, Daniel E. Leaird, Nan-Wei Chen (ID), Jin-Wei Shi (ID), *Senior Member, IEEE*, and Andrew M. Weiner (ID), *Fellow, IEEE*

Abstract—Millimeter wave (MMW) sensing systems have potential for enhanced range and angular resolution in comparison to lower radio frequencies. This article employs photonic-assisted radio-frequency arbitrary waveform generation to implement a high-bandwidth multi-target MMW radar. The presented sensing system operates in the W-band using chirped RF signals, with spectra between 80 and 95 GHz at the 10 dB points. We implement sum- and difference-mode beamforming using a two element transmitter array to perform azimuth angle sensing in addition to target ranging. Photonics-based waveform generation with programmable optical pulse shapers provides for incorporation of approximately uniform phase shifts across the entire bandwidth, which in turn enables control of the far-field interference patterns of the broadband waveforms. Our approach has analogies with monopulse tracking radar techniques, in which target angle information is revealed through sum- and difference-mode processing of the receiving antennae, but with the dual-mode processing implemented at the transmitter side via photonic radio-frequency arbitrary waveform generation. Experiments with a single target demonstrate unambiguous sensing of target angle with an estimated root-mean-square error of 0.18° over a ±4° angular range. We also demonstrate independent sensing of the angles of two targets that are resolved in range.

Index Terms—Frequency-to-time mapping, microwave photonics, millimeter wave sensing, monopulse reception, optical pulse shaping, photonic radar, photonic-assisted arbitrary waveform generation, sum and difference beamforming, W-band, RF photonics.

I. INTRODUCTION

THE research related to millimeter wave (MMW) and sub-terahertz (sub-THz) frequencies has developed significantly in recent decades. To mitigate the spectral congestion in lower radio-frequency (RF) bands, MMW frequency regions with broader bandwidths can be accessed for applications like high-resolution ranging [1], [2], ultrahigh-speed wireless communication [3]–[8], and electromagnetic imaging [9], [10]. Conventional sensing systems working in the frequency region below 30 GHz face challenges in detection and high resolution imaging of small targets [11]. Shorter wavelengths in the MMW region from 30 to 300 GHz (1 cm to 1 mm) can provide better angular resolution and can support ultrabroad bandwidth favoring high resolution ranging. These qualities make MMW 3-dimensional (3-D) radars promising for use in self-driving vehicles [12] and intelligent driver assistance systems [13].

Several approaches have been previously explored to accomplish 3-D imaging with high angular resolution. A quasi-optics approach was demonstrated based on a MMW/THz lens (or parabolic mirror) [1], [14] to focus and narrow down the RF beam for improved transverse resolution. However, the sensing distance at which full azimuth and range resolution is maintained is fixed by the working distance of the focusing element. True time delay beamforming in phased array systems can provide range and angle sensing over large working distances. However, conventional implementations with electronic devices limit the bandwidth supported in these systems. Range resolution can be enhanced by techniques allowing versatile ultrabroadband phase shifting and waveform generation. Microwave photonic technologies have been extensively explored for this purpose [15]–[17]. A photonics-based true time delay phased array radar demonstrated recently used digital beamforming [18] to cover a 22–26 GHz frequency band and achieved range and azimuth resolution of 3.85 cm and 2.68°, respectively.

The work we report here is based on photonic assisted radio-frequency arbitrary waveform generation (RF-AWG) [19]. Photonic-assisted RF-AWG [19] based on optical pulse shaping [20] and frequency-to-time mapping [21]–[23] has achieved programmable arbitrary waveform generation both at baseband and at center frequencies up to the low MMW regime, with bandwidths as large as 50 GHz [24]. In [2] photonic assisted RF-AWG was extended to the W-band (75–110 GHz) using a near-ballistic uni-traveling-carrier photodiode (NBUTC-PD) based photonic transmitter-mixer (PTM) [25] for photodection. Ranging experiments conducted using waveforms spanning most of the W-band demonstrated range resolution down to several millimeters [2]. Here we apply photonic RF-AWG for driving a two-element transmitter array in the W-band to achieve simultaneous range and angle sensing. Our approach is inspired by monopulse

radar tracking techniques, in which target angle information is revealed through simultaneous processing of sum and difference patterns using beamforming networks following an array of receiving antennae [13], [26]–[28]. In our scheme, sum and difference mode waveforms are sequentially transmitted from a (two element) antenna array and echo signals received by a single antenna are post-processed to retrieve the target angle. Sum and difference mode transmission is implemented by programming a pair of pulse shaper based photonic RF-AWG units to generate a pair of broadband waveforms that are alternately in phase and out of phase respectively. The ability of photonics-based waveform generation to impose an approximately uniform phase shift and control the far-field interference across the entire bandwidth is a key enabler for this approach. Compared to traditional monopulse radar which uses narrowband pulses, our approach based on ultrabroadband pulse compression can provide much better range resolution.

In this paper we report a two-dimensional photonic-assisted radar which utilizes a pair of W-band chirped waveforms with ∼15 GHz 10 dB bandwidths for simultaneous range and angle sensing. Experiments with a single target demonstrate unambiguous sensing of target angle with an estimated RMS error of 0.18° over a ±4° angular range. Although our angle sensing method is predicated on the presence of a single isolated target, it can also be applied to two or more targets, provided that the targets are clearly resolved in range. With our experimental parameters we can achieve range resolution of 1.5 cm for a single target; accurate sensing of the angles of two independent targets is demonstrated for a somewhat larger range difference of 2.5 cm. To our knowledge our work constitutes the first broadband photonics-assisted radar based on sum and difference transmission beamforming. Our scheme can potentially be extended to a four-element transmitter array for sensing in three dimensions (angle in both horizontal and vertical planes, plus range). In addition, this approach should offer advantages that are associated generally with radio-frequency photonics, such as reduced susceptibility to electromagnetic interference, low propagation loss in radio-over-fiber signal distribution and low timing jitter. Our work has potential relevance for photonically distributed, multi-antenna millimeter wave radar, which has been explored for applications both to self-driving cars [29] and to surveillance of obstacles and debris in airport runways [30], [31], and possibly to millimeter wave synthetic aperture radar that uses monopulse processing for ground moving target indication [32].

While the current experiments are set for operation in the W-band, the waveform generation technique can be configured for both larger bandwidths and higher center frequencies, provided that appropriate photomixers and RF components are available. An analysis of RF bandwidths and time-bandwidth products attainable using the frequency-to-time mapping technique is given in [21].

The rest of this paper is organized as follows. In Section II we discuss the experimental apparatus for waveform generation and transmission mode beamforming. We also demonstrate control of broadband constructive and destructive interference along the transmission center axis. Section III presents a theoretical analysis of the angular dependent far-field interference under sum and difference mode transmission as well as experiments that confirm the theoretical predictions. Section IV extends these results to a pulse compression radar scenario for simultaneous range and angle sensing. Our treatment first outlines the signal processing procedures and then characterizes experimental performance in both single target and multiple target operation. Finally, in Section V we summarize and discuss ideas for future enhancements.

Preliminary experimental results on broadband far-field interference control and target sensing were reported in conference publications [33] and [34], respectively. Here for the first time we formulate the theory for the angular-dependent far-field waveforms and for the pulse compression processing procedure that allow us to extract simultaneous range and angle information and present comprehensive experimental results.

II. EXPERIMENTAL SETUP

Fig. 1 illustrates our experimental setup for W-band transmitter array beamforming. It consists of three sections: photonic-assisted arbitrary waveform generation (AWG), fast photodetection, and wireless antenna array channel. In the experiment, the optical pulse from the laser source is stretched in time by a dispersive fiber, with 37.5 ps/nm total dispersion. After the input pulse passes through the dispersive fiber, it is divided into two arms by a fiber splitter and spectrally shaped by pulse shapers to result in two optical waveforms with time domain structure being scaled replicas of the original optical power spectrum. The pulse shapers are programmed based on the near-field frequency-to-time mapping technique [21] to modulate the optical spectrum of the mode-locked laser, in order to generate the user defined optical profiles, which are later converted to desired W-band waveforms through photodetection. The pulse shapers used in the setup are Finisar WaveShapers, covering the entire optical C-band (1525-1565 nm, ∼5 THz optical bandwidth, ∼10 GHz 3 dB spectral resolution). The optical signals from the photonic-assisted AWG are converted to millimeter-waves (MMWs) by two UTC-PDs based waveguide-coupled photomixers - one of them homemade [25], and the other obtained commercially (NTT Electronics IOD-PMW-13001). They are connected to two identical horn antennas (Millitech SGH-10-RP000) which are placed side-by-side separated by $d \approx 2.3$ cm, to serve as the transmitter block. A third horn antenna (QuinStar Technology, Inc. W-band QWH-WPRR0) serving as the receiver, is initially placed on a swing arm controlled by a programmable translation stage, to demonstrate sum and difference mode beamforming pattern as a function of angle. The antenna is located 3 meters away, facing the two transmitters. However, as described later in Section IV, to demonstrate remote target sensing, the receiving antenna is later relocated close to transmitter array. All three antennas have 20 dB antenna gain across the W-band. For a larger field of view, lower gain antennas such as patch antennas could be used instead. The photonic assisted AWG is applied to generate the linearly chirped W-band waveforms with 1.5 ns time duration and 3 dB bandwidth of 6 GHz (covering 80 to 95 GHz within 10 dB). The waveforms have a repetition period
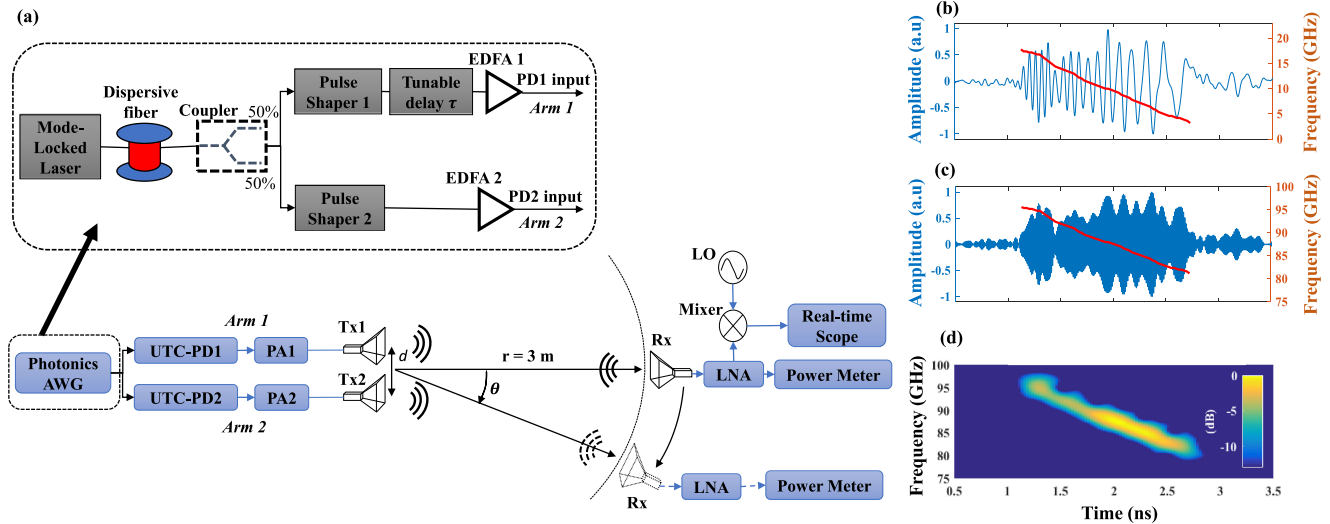
Fig. 1. Experimental diagram and wireless W-band ultrabroadband chirped waveform transmission. (a) Experimental setup for beamforming, with receiver antenna located at far field. AWG, arbitrary waveform generation; UTC-PD, uni-traveling carrier photodiode based waveguide-coupled photomixer; PA, power amplifier; Tx, transmitter antenna; Rx, receiver antenna; LNA, low noise amplifier; LO, local oscillator; d = 2.3 cm, r = 3 m (b) Received down-converted chirped signal radiated from a single transmitter antenna and its instantaneous center frequency. The waveform with ∼ 15 GHz 10-dB bandwidth (linear chirp, 80–95 GHz) is sampled by the real-time scope at the receiver end after down-conversion by 78 GHz. (c) Reconstructed received W-band chirped signal and its instantaneous center frequency. (d) Spectrogram of waveform in (c).

of 4 ns equal to that of mode-locked laser (MLL), which sets the unambiguous range detection window.

The signal detected by the receiving antenna is forwarded to a low noise amplifier (Millitech LNA-10-02150) with ∼23 dB gain over a frequency range of 80-105 GHz. Based on the requirement of the experiment, the received and amplified W-band waveform is either sent for time-resolved measurement or to an RF power meter. For time-resolved operation, the LNA is connected to a second harmonic mixer with ∼17 GHz intermediate frequency (IF) bandwidth, which down-converts the received signal by 78 GHz (the local oscillator driving the mixer is at 39 GHz). Following this, the down-converted waveform is recorded by a real-time oscilloscope with 20 GHz analog bandwidth and 50 GS/s sampling rate. The MLL repetition rate, real-time scope and the local oscillator are synchronized to a common clock.

Waveforms shown in Figs. 1 and 2 are measured under time-resolved operation. Fig. 1(b) shows the down-converted signal with the instantaneous frequency when only one of the transmitters is enabled and the receiving antenna is placed on the bore-axis (i.e angular displacement $\theta = 0$) in the far field. The reconstructed W-band waveform shown in Fig. 1(c) is calculated offline by up-converting the spectrum of waveform in Fig. 1(b) by 78 GHz. Fig. 1(d) shows the spectrogram of the linearly chirped reconstructed W-band waveform in Fig. 1(c). We first investigate the sum (Σ) and difference (Δ) transmission beamforming along the bore-axis of the transmitter array in Fig. 2, with the receiver stage in time-resolved operation. The receiver antenna is initially set on the bore-axis with no angular offset ($\theta = 0°$) and transmitted waveforms are measured using the real-time scope when one of the transmitters is enabled at a time. The pulse shapers in the two arms (shown in Fig. 1(a)) are programmed to impose either same or opposite polarities on
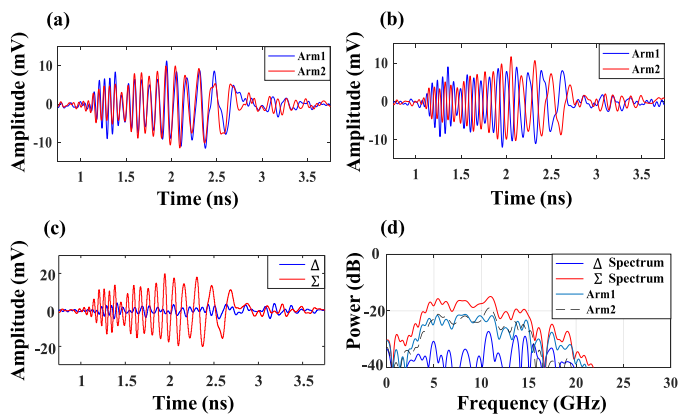

Fig. 2. Photonic monopulse transmitter array beamforming time domain waveforms measurement (center axis). (a) Down-converted waveform at Rx when only Tx_1 is radiating (blue), when only Tx_2 is radiating (red). Waveforms feeding Tx_1 and Tx_2 are in phase. (b) Similar to (a) but waveforms feeding to Tx_1 and Tx_2 are out of phase by π rad. (c) Down-converted Σ (red) and Δ (blue) interference waveforms at Rx with both Tx_1 and Tx_2 radiating. (d) Spectra of received single transmitter signals and Σ- and Δ-mode signals; red trace, Tx_1 and Tx_2 are both radiating in the Σ transmission mode (in phase); blue trace, Tx_1 and Tx_2 are both radiating in Δ transmission mode (out of phase); green trace, only Tx_1 is radiating; black trace, only Tx_2 is radiating.

the waveforms (in addition to spectrally shaping the dispersed modelocked pulses).

Figs. 2(a) and 2(b) show the received downconverted RF waveforms for W-band transmission with either the same or the opposite polarities. Fig. 2(c) shows the downconverted waveforms received at $\theta = 0°$ when both the transmitting antennas are radiating simultaneously. When both transmitted waveforms have the same polarity (red, Σ-mode), constructive interference occurs and we observe amplitude doubling in the received waveform. When the interfering signals have opposite polarity (blue,

Δ-mode), destructive interference occurs, resulting in near-zero amplitude over the entire time aperture. The RF power spectra of waveforms in Figs. 2(a)-(c) are computed offline and shown in Fig. 2(d). The extinction ratio between Σ- and Δ-mode spectra averaged over 2–17 GHz (corresponding to 80–95 GHz in the W-band) is 15.96 dB. The Σ-mode power spectrum is $\sim$6 dB stronger than that of either single-Tx spectrum, consistent with the amplitude doubling evident in Fig. 2(c). These results clearly demonstrate the ability of our photonics-based generation approach to impose an approximately uniform phase shift and control the far-field interference across the entire bandwidth.

III. Sum (Σ) and Difference (Δ) Transmission Mode Interference

A. Theoretical Background

The W-band waveforms generated in our experiment are linearly chirped in frequency as shown in Fig. 1(d). However, our approach should also work for other broadband waveforms. In general, the electric field of a broadband W-band waveform with carrier angular frequency ω_0 and complex amplitude $a(t)$ can be expressed as

$$V_W(t) = \frac{1}{2}[a(t)e^{j\omega_0 t} + c.c.] \qquad (1)$$

Transmitters (Tx_1 and Tx_2), shown in Fig. 1(a), are separated by a distance d, and placed symmetrically with respect to the axis. The transmitters are operated in the Σ- or Δ-mode and respective transmitted waveforms (T_i^Σ and T_i^Δ, $i = 1, 2$) follow the relation,

$$T_2^\Sigma(t) = T_1^\Sigma(t) = \mathrm{Re}[a(t)e^{j\omega_0 t}], \qquad (2)$$

$$T_2^\Delta(t) = -T_1^\Delta(t) = -\mathrm{Re}[a(t)e^{j\omega_0 t}]. \qquad (3)$$

The receiver is placed at a range r from the origin, making an angle θ with the center axis of the transmitter array. As shown in Fig. 1(a), the receiver is defined to have a positive angular shift when located closer to transmitter 2 compared to transmitter 1. Under the far field condition, the waveform transmitted from Tx_1 (Tx_2) to the receiver is delayed (advanced) by $\tau_\theta \equiv \frac{d\sin\theta}{2c}$ as compared to a scenario where the waveform is emitted from the origin. In our experiments, the transmitting antennae have apertures $b = 1.87$ cm with center-to-center separation $d \approx 2.3$ cm in the horizontal plane, for a total aperture $b + d \approx 4.17$ cm. The receiver is at distance of $r \approx 3$ m from the origin. The W-band power spectrum covers a frequency range from 80 to 95 GHz with a mean frequency of 86.5 GHz (~ 3.5 mm mean wavelength, λ), taken to be the center carrier frequency ($\omega_0/2\pi$). Together, these values satisfy the far field regime conditions, $r \gg \frac{2(b+d)^2}{\lambda}$, $r \gg b + d$ and $r \gg \lambda$.

The W-band waveforms $S_{\omega_0}(t, r, \theta)$ and $D_{\omega_0}(t, r, \theta)$, observed by a receiver placed at angle θ in the far field under Σ- and Δ-mode transmission respectively, are written

$$S_{\omega_0}(t, r, \theta) = k_\theta \left[T_1^\Sigma(t' - \tau_\theta) + T_2^\Sigma(t' + \tau_\theta) \right]$$

$$= k_\theta \, \mathrm{Re} \left[a(t' - \tau_\theta)e^{j\omega_0(t' - \tau_\theta)} + a(t' + \tau_\theta)e^{j\omega_0(t' + \tau_\theta)} \right] \quad (4)$$

$$D_{\omega_0}(t, r, \theta) = k_\theta \left[T_1^\Delta(t' - \tau_\theta) + T_2^\Delta(t' + \tau_\theta) \right]$$

$$= k_\theta \, \mathrm{Re} \left[a(t' - \tau_\theta)e^{j\omega_0(t' - \tau_\theta)} - a(t' + \tau_\theta)e^{j\omega_0(t' + \tau_\theta)} \right] \quad (5)$$

where $t' = t - \frac{r}{c}$ is a function of receiver distance r and incorporates the fixed delay when a waveform is emitted from the origin and reaches the receiver. k_θ is the proportionality constant including angular response of transmitting and receiving horn antennae.

As explained below, we are primarily interested in small angles, $-5° \leq \theta \leq 5°$, for which the delay parameter τ_θ satisfies $\tau_\theta \leq 3.3$ ps. Since this is much smaller than the inverse bandwidth of our W-band waveforms, $a(t)$ can be assumed to be slowly varying on the scale of τ_θ. We may therefore make the approximation

$$a(t + \tau_\theta) \approx a(t) \approx a(t - \tau_\theta). \qquad (6)$$

By using this simplification in Eqs. (4–5) and writing $a(t)$ as $|a(t)|e^{j\alpha(t)}$, we obtain the following expressions for the W-band waveforms at the receiver

$$S_{\omega_0}(t, r, \theta) = 2k_\theta |a(t')| \cos(\omega_0 \tau_\theta) \mathrm{Re}[e^{j(\omega_0 t' + \alpha(t'))}] \qquad (7)$$

$$D_{\omega_0}(t, r, \theta) = 2k_\theta |a(t')| \sin(\omega_0 \tau_\theta) \mathrm{Re}[-je^{j(\omega_0 t' + \alpha(t'))}] \qquad (8)$$

Angular information may be obtained from the $\cos(\omega_0 \tau_\theta)$ and $\sin(\omega_0 \tau_\theta)$ terms in Eqs. (7–8). The angle may be determined unambiguously for $|\omega_0 \tau_\theta| \leq \pi/2$. Using 86.5 GHz as the center frequency, this corresponds to $|\tau_\theta| \leq 2.9$ ps and $|\theta| \leq 4.4°$, justifying our assumptions.

Following this, the W-band waveforms are downconverted by the LO frequency ω_{LO} before being recorded by the real-time scope. This can be evaluated by multiplying the expression inside the $\mathrm{Re}[\ldots]$ in Eqs. (7) and (8) by $e^{-j\omega_{LO}t}$

$$S_{\omega_c}(t, r, \theta) = 2k_\theta |a(t')| \cos(\omega_0 \tau_\theta) \mathrm{Re}[e^{j(\omega_c t' + \alpha(t') - \varphi_r)}] \quad (9)$$

$$D_{\omega_c}(t, r, \theta) = 2k_\theta |a(t')| \sin(\omega_0 \tau_\theta) \mathrm{Re}[-je^{j(\omega_c t' + \alpha(t') - \varphi_r)}] \qquad (10)$$

where $\omega_c = \omega_0 - \omega_{LO}$ and $\varphi_r = \frac{\omega_{LO} r}{c}$.

In target sensing experiments described later in Section IV, the received down-converted waveforms are reconstructed offline to W-band during post-processing (by shifting all positive frequencies in the Fourier transform of the downconverted waveforms by ω_{LO}, and negative frequencies by $-\omega_{LO}$). This is equivalent to multiplying the quantity inside $\mathrm{Re}[\ldots]$ in Eqs. (9) and (10) by $e^{j\omega_{LO}t}$. Thus the reconstructed W-band waveforms can be written

$$S_{\omega_0}(t, r, \theta) = 2k_\theta |a(t')| \cos(\omega_0 \tau_\theta) \cos(\omega_0 t' + \alpha(t')) \quad (11)$$

$$D_{\omega_0}(t, r, \theta) = 2k_\theta |a(t')| \sin(\omega_0 \tau_\theta) \sin(\omega_0 t' + \alpha(t')) \quad (12)$$

B. Analysis of Σ- and Δ-Mode Waveforms

We now draw on this analysis to discuss the angular dependence of Σ- and Δ-mode data in experiments.

First, Σ- and Δ-mode far-field patterns are acquired by recording the received power (measured with the RF power meter, see Fig. 1) as the receiving antenna is swept over an arc in steps from
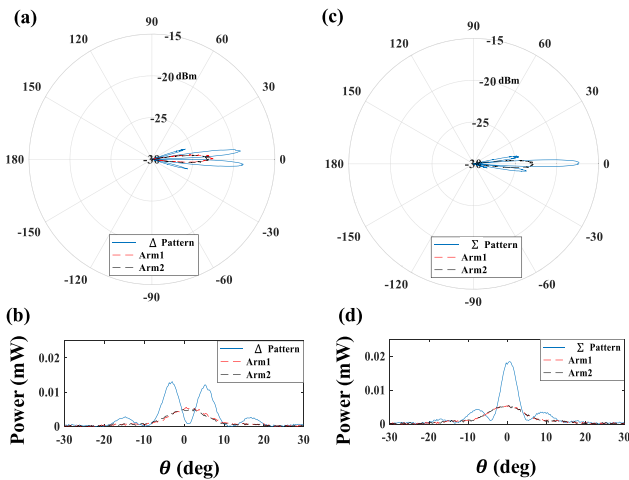
Fig. 3. Far field antenna pattern measurement for Σ and Δ pattern beamforming. (a,b) Far field broadband antenna array pattern with Tx_1 and Tx_2 in Δ transmission mode (out of phase). Polar plot with log scale in (a) and Cartesian plot with linear scale in (b). (c,d) Far field broadband antenna array pattern with Tx_1 and Tx_2 in Σ transmission mode (in phase). Polar plot with log scale in (c) and Cartesian plot with linear scale in (d). The measured powers at $\theta = 0^\circ$ are $0.65\,\mu W$ and $22.1\,\mu W$ for Δ and Σ transmission modes, respectively; the power at $\theta = 0^\circ$ with only a single transmitter enabled is $5.81\,\mu W$.

$\theta = -30^\circ$ to $+30^\circ$ with a 0.25° angular increment. The far-field antenna pattern is also measured with one arm transmitting at a time. The measured patterns of W-band power as a function of receiver angular shift are plotted in Figs. 3(a-d). In the Δ transmission mode, the polar (Fig. 3(a)) and Cartesian (Fig. 3(b)) plots show a null at the center. In contrast, when the transmitters emit signals with the same polarity, a constructive interference peak is observed at $\theta = 0^\circ$ in Figs. 3(c) and 3(d). An extinction ratio of 15.31 dB between the Σ- and Δ-patterns at $\theta = 0^\circ$ is observed, in agreement with the extinction ratio estimated from the time domain data (Fig. 2).

Fig. 4 shows examples of down-converted time domain waveforms measured with the receiver stage off-axis in time-resolved operation. The examples compare the phase relation between Σ- and Δ-mode waveforms, for both positive and negative receiver angular shifts. Some of the key points are as follows :

- The experimental Σ and Δ interference patterns in Fig. 3 exhibit an angular fringe period of 8.8^o (angular spacing between peaks in Δ-mode and zeroes in Σ-mode). Using the $\cos(\omega_0 \tau_\theta)$ and $\sin(\omega_0 \tau_\theta)$ terms in Eqs. (7 - 12), and center carrier frequency of 86.5 GHz, the angular fringe period of 8.8° gives a precise estimate of separation between transmitting antennae to be $d = 2.26$ cm. Within one angular fringe period, the absolute value of the receiver angular shift can be determined uniquely from the ratio of powers received in Σ- and Δ-mode transmission.
- The Σ- and Δ-mode waveforms at a given receiver angle are in quadrature phase with each other. From Figs. 4(a) and 4(b), we observe that the Δ-mode (red) waveform leads the Σ-mode waveform (blue) for negative receiver angles and lags the Σ-mode waveform for positive receiver angles. This lead-lag phase relation is predicted by the equations and is an indicator of the direction of angular shift.

- The equations predict that Σ-mode waveforms measured by receivers at fixed range and equal but opposite angles should be identical. The Δ-mode waveforms for equal but opposite angles should have a relative phase difference of π. However, to observe these features experimentally, we must account for the mm-scale range variations that occur when we mechanically sweep the receiver angle (such variations affect the φ_r term in Eqs. (9–10)). Here we use a Σ-mode waveform pair at equal but opposite angular shifts, $S_{\omega_c}(t, r_1, \theta)$ and $S_{\omega_c}(t, r_2, -\theta)$, as a reference. That is, in the Σ-mode data of Figs. 4(d) and 4(f), corresponding to $\theta = \pm 3^\circ$ and $\pm 7.5^\circ$ respectively, in each case we shift the phase of one of the waveforms to match that of the other. The same phase shift is then applied to the corresponding Δ-mode waveform. The results are plotted in Figs. 4(c) and 4(e). In both cases the Δ-mode waveforms at equal but opposite angular shifts are clearly out of phase, as predicted.

We can deduce from the above analysis that the receiver angular shift can be retrieved from Σ- and Δ-mode waveforms. In the following section, we extend our experiments to realize range and angle sensing of multiple targets.

IV. HIGH RESOLUTION REMOTE TARGET(S) SENSING

Our photonic radar system consists of a two element antenna array that transmits alternately in Σ- and Δ-modes and a single receiving antenna, as illustrated in Figs. 5(a) and 6(a). This is in contrast to the traditional monopulse tracking radar concept, which switches between Σ- and Δ-modes [27], [35] using an array receiver. The receiver block from the setup in Fig. 1 is relocated close to the transmitting antennae and placed on the line bisecting the transmitter array such that the bore-axis is normal to the plane containing the three antennae (see figures). Now the mechanical swinging arm is used to move a (4 in by 4 in) metal plate referred as Target 1 along a 3-meter radius arc from $\theta = -4^\circ$ to 4° in 0.1° angular increments. A second identical sized target referred as Target 2 is placed approximately on-axis in later multi-target sensing experiments.

A. Single Target Sensing

At the outset we consider single target sensing with Target 1 only (Target 2 is not present). The analysis of Σ- and Δ-mode waveforms from Section III can be extended to single target echo waveforms under a few conditions - (i) the reflectance of the target is uniform over all transmitted frequencies, and (ii) the target aperture is small enough (given our targets at range ≥ 3 m) such that reflected response does not have to be integrated over a range of angles. The received downconverted echo waveforms from a target at range r and angle θ take the same form as Eqs. (9) and (10) but follow the relation, $t' = t - \frac{2r}{c}$ due to the round trip distance travelled by the waveforms in the radar configuration. The constructive and destructive interference in Σ- and Δ-modes when the target is placed at the center axis of the transmitter array (antenna boresight) is shown in Fig. 5(b). Examples of experimental Σ and Δ echo waveforms for $\theta = \pm 2.3^\circ$ are shown in Figs. 5(c) and 5(d). The lead-lag phase relation
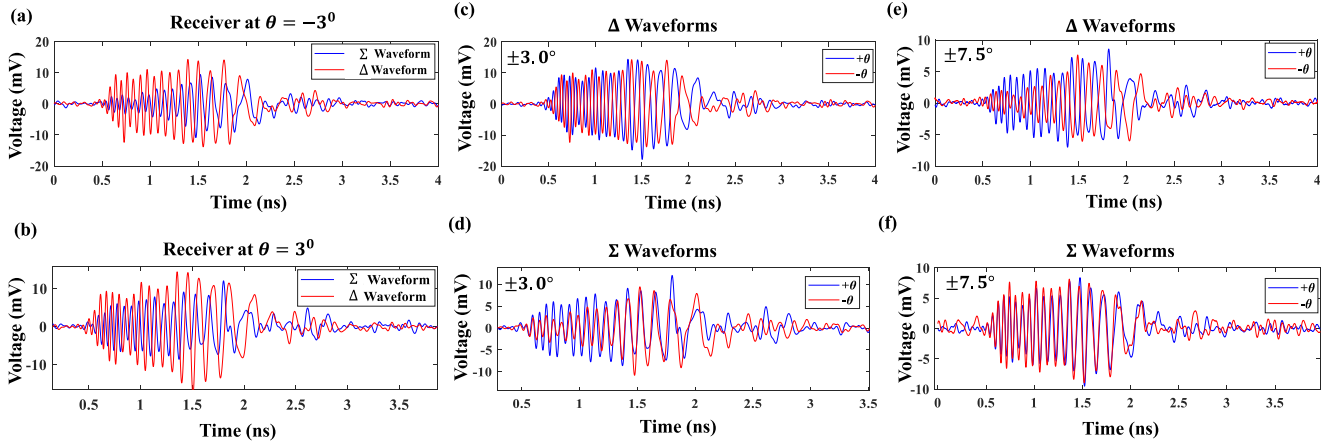
Fig. 4.   Far field off-axis antenna time domain waveforms measurement. Examples of received downconverted Σ and Δ mode waveforms when Rx is located at angular displacement of (a) -3° and (b) $+3^o$. The Σ and Δ mode waveforms are in quadrature phase with each other at a given receiver angle. Examples of received downconverted waveforms for Δ transmission when Tx_1 and Tx_2 are set out of phase with Rx located at angular displacement of (c) $\pm3°$, (e) $\pm7.5°$. Examples of received downconverted waveforms for Σ transmission when Tx_1 and Tx_2 are in phase with Rx located at angular offset (d) $\pm3°$ and (f) $\pm7.5°$.
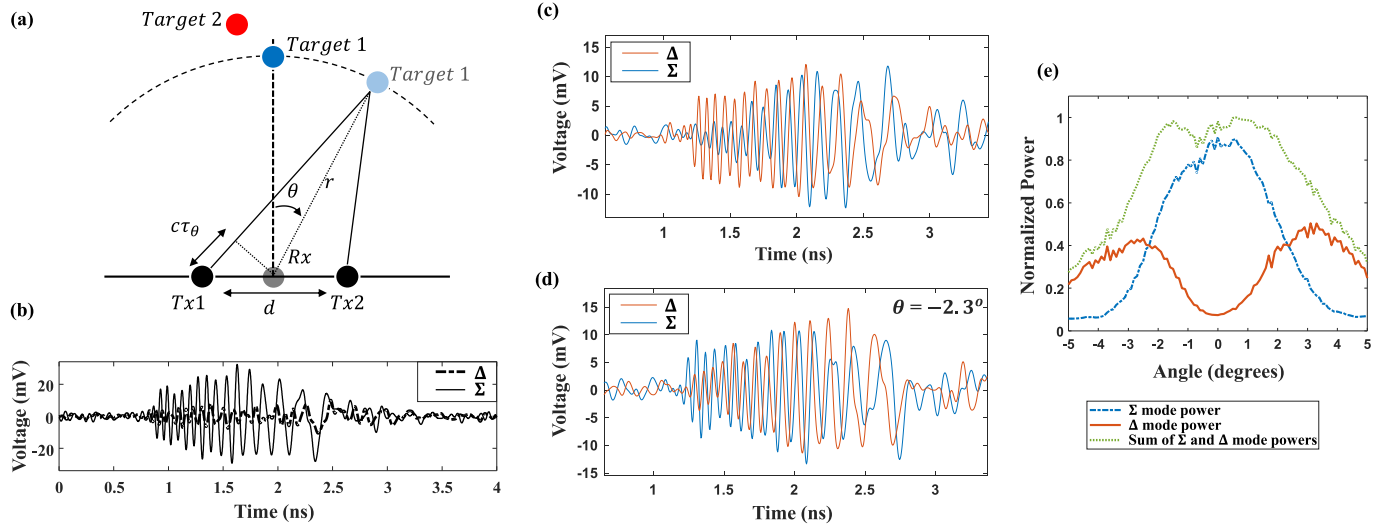

Fig. 5.   (a) Experimental scheme for target(s) sensing. Examples of downconverted received Σ- and Δ-mode waveforms, reflected from a single target located at (b) center axis, (c) $+2.3°$, and (d) $-2.3°$. (e) Received echo power under Σ and Δ transmission modes, and sum of their powers with single target placed in the far field.

between the Σ and Δ echo waveforms and its dependence on the direction of target angular shift is consistent with the discussion in the previous section.

The integrated power in the reflected waveforms is plotted as a function of single target angle in Fig. 5(e). The total power (green curve) by adding Σ- and Δ-mode powers, is approximately flat over the central $\pm2°$ and then rolls off, reflecting the angular response of our antennae.

As discussed in Section III, the amplitudes of the Σ- and Δ-mode echo waveforms reveal the absolute value of azimuth angle and the relative phase between them reveals the direction of angular shift.

To proceed, the received waveforms are first apodized by a flat-topped window function of 4 ns total duration, with 0.8 ns rise and fall times. Any effect of nonequal transmitted powers by the two arms is rectified by back-calculating the two transmitted

waveforms from the received Σ and Δ waveforms ($a(t)$ in Eq. (1), but now allowed to be slightly different for the two transmitters) and normalizing the power calculated for each transmitter to unity. Our estimates for the Σ and Δ echo waveforms are then updated by calculating the sum and difference of the so-normalized transmitted waveforms, after which they are reconstructed to W-band. This normalization procedure is observed to improve angle sensing accuracy in dual target experiments but has little effect in the single target experiments.

Pulse compression is essential in order to achieve the potential range resolution. We perform this compression offline by computing the cross-correlation of the reconstructed W-band Σ- and Δ-mode echo waveforms with a real reference signal $\mathcal{V}_{\omega_0}(t)$. We record a downconverted waveform reflected from a target placed on the transmitter array axis in the far field at a distance r_{ref} and up-convert it to W-band offline to obtain the reference.
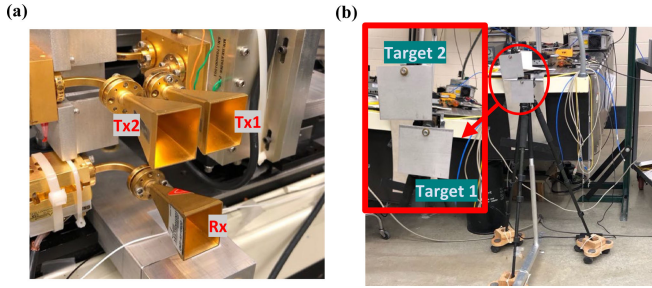
Fig. 6. (a) Transmitter and receiver antenna blocks for target detection. Tx_1 and Tx_2 are separated in horizontal direction by $d \approx 2.3$ cm. Rx is placed close to and equidistant from the transmitters. (b) Targets placed at far field, 3 meters away from the transmitter and receiver block.

That is,

$$\mathcal{V}_{\omega_0}(t) = S_{\omega_0}(t, 2r_{ref}, \theta_{ref} = 0). \tag{13}$$

The cross-correlations of each of the Σ and Δ echo waveforms with the reference $\mathcal{V}_{\omega_0}(t)$ are computed. The cross-correlation waveforms at carrier frequency of ω_0 for a single target at range r and angle θ are given by

$$X_\Sigma(\tau; \omega_0) = \int S_{\omega_0}(t + \tau, 2r, \theta)\mathcal{V}_{\omega_0}(t)dt \tag{14}$$

$$X_\Delta(\tau; \omega_0) = \int D_{\omega_0}(t + \tau, 2r, \theta)\mathcal{V}_{\omega_0}(t)dt \tag{15}$$

The relative phase between Σ- and Δ-mode waveforms is preserved upon compression, since a common reference is used for cross-correlation. Figs. 7(a,b) show W-band compressed waveforms obtained using return data from a single target placed at angles $\theta = \pm 3.1°$ respectively. Compressed waveforms for Σ- and Δ-mode have essentially identical envelopes, as expected under the slowly varying envelope approximation of Eq. (6), with durations equivalent to roughly ten periods of the W-band carrier. However, the amplitudes and phases of the compressed waveforms differ; these differences are the signature of the target angle. The lead-lag phase relation between Σ- and Δ-mode waveforms is the same as in Fig. 5(c,d); i.e., for negative θ the Δ-mode waveform leads the Σ-mode waveform, and vice versa for positive θ. For illustration, in Figs. 7(c,d) we also plot the compressed down-conversion waveforms. Because the resulting compression peaks comprise only a single cycle of the down-converted carrier, the lead-lag phase relation between Σ- and Δ-mode waveforms is more clearly visualized.

We utilize this lead-lag relation to determine the sign of the target's angular position, θ. Our procedure is to compute the cross-correlation between the Σ-mode compression trace $X_\Sigma(t; \omega_0)$ and the Δ-mode compression trace $X_\Delta(t; \omega_0)$. The sign of the time delay at which a peak occurs in this cross-correlation of compression traces gives the sign of θ. The absolute values of the peak amplitudes of the compressed waveforms (which we term $|A_S|$ and $|A_D|$ respectively) can be used to extract the absolute value of θ,

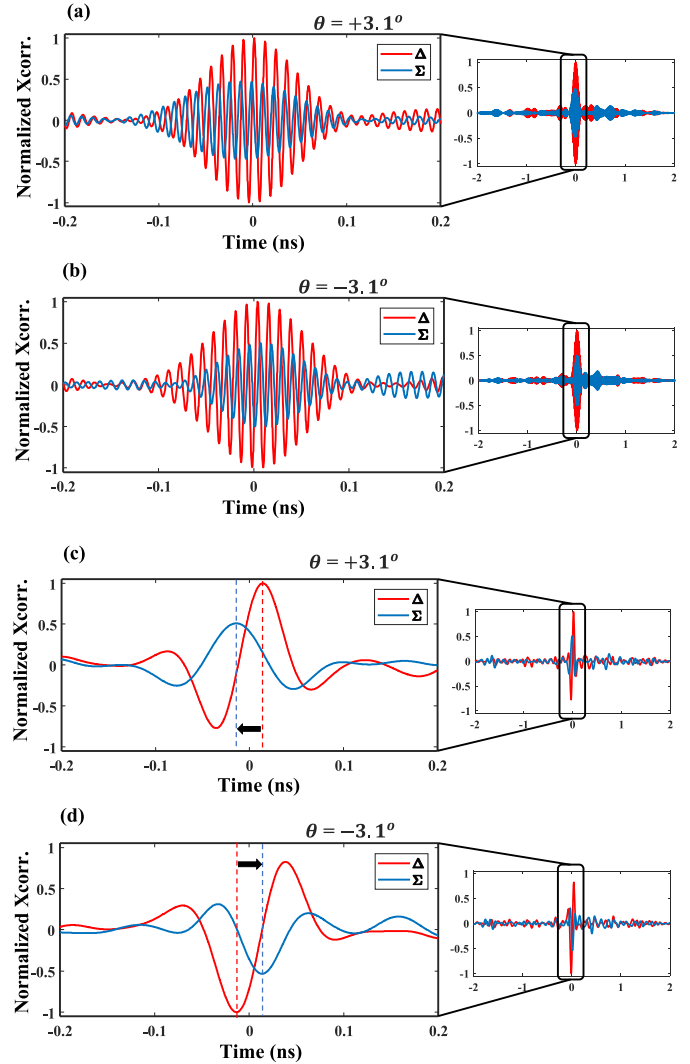$$|\theta| = \frac{2c}{\omega_0\, d}\arctan\left(\frac{|A_D|}{|A_S|}\right) \tag{16}$$

Fig. 7. Example of single target Σ and Δ reconstructed W-band compression traces for (a) $+3.1°$, (b)$-3.1°$. The respective compression waveforms in downconverted regime are plotted in (c) and (d) for better illustration of the lead-lag phase relation.

where the values of the constants have been given previously. The angles retrieved when a single target is swept over the range $-4°$ to $4°$ are shown in Fig. 8(a). Here the horizontal axis corresponds to the actual target angle assuming that the mechanical swing arm executes an ideal angular sweep with uniform $0.1°$ increments. For the most part, the retrieved angle is linear in the actual target angle with slope one. Retrieved angles close to $\theta = 0°$ have higher error because the expected extinction of the Δ-mode signal near $0°$ makes it more sensitive to noise—see dual target sensing section for further discussion. Nevertheless, the root-mean-square (RMS) error of retrieved single target angles over the angular span is only $0.18°$.

B. Dual Target Sensing

In this section we discuss range and azimuth sensing of two independent targets. As sketched in Fig. 5(a), Target 1 is moved over an arc of constant radius about the center of the transmitter
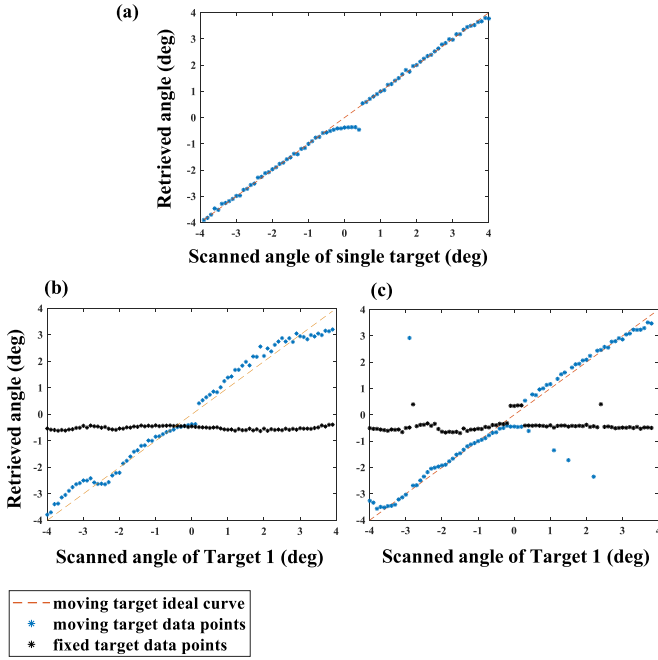
Fig. 8. Retrieved single target angular displacement (a) and retrieved dual target angular displacements when the targets are separated by (b) 4.7 cm (c) 2.5 cm.
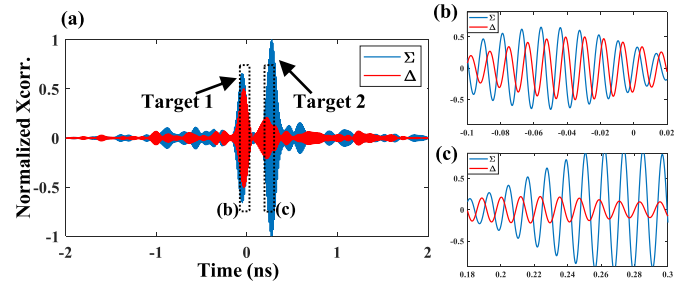

Fig. 9. (a) Example of dual target reconstructed W-band compression traces for (moving) Target 1 at positive angular shift of 1.4^o and (stationary) Target 2 at negative angular shift of -0.5^o. The expanded views in (b) and (c) show the carrier lead-lag relation for (b) Target 1 and (c) Target 2 compression peaks, respectively. The range separation between the two targets in this example is 4.7 cm.

array, while target 2 remains stationary. The post-processing employed for single target angle sensing can be extended to the dual-target (and potentially multi-target) scenario. However, the performance of our angle sensing scheme is contingent on being able to resolve different targets in range. That is, if the range of the targets are not sufficiently different, the angle retrieval is compromised.

Let the depth and angular displacement of the moving target and the stationary target be (r_1, θ_1) and (r_2, θ_2), respectively. The dual target Σ- and Δ-mode echo fields (S^d and D^d) are equal to the sum of the contributions from individual targets.

$$S^d_{\omega_0}(t) = S_{\omega_0}(t, 2r_1, \theta_1) + S_{\omega_0}(t, 2r_2, \theta_2) \qquad (17)$$

$$D^d_{\omega_0}(t) = D_{\omega_0}(t, 2r_1, \theta_1) + D_{\omega_0}(t, 2r_2, \theta_2) \qquad (18)$$

The round trip distances travelled by the W-band waveforms are taken into consideration to express the above dual target echo fields. Here S_{ω_0} and D_{ω_0} are the individual target Σ- and Δ-mode fields given by Eqs. (11–12).

1) Azimuth Estimation: Similar to the single target scenario, the W-band compression waveforms are employed to estimate the azimuth angle. Σ- and Δ-mode return signals are cross-correlated with a single reference waveform $\mathcal{V}_{\omega_0}(t)$ similar to Eqs. (13–15). This results in compression, with two peaks corresponding to the two targets. The temporal separation between the compression peaks reflects twice the difference in target ranges; as before, the amplitudes of Σ- and Δ-mode signals within an individual peak carry information on the individual target angles. The ratio between absolute values of Σ- and Δ-mode compression peak amplitudes is computed for each range-resolved target and $|\theta|$ is retrieved using Eq. (16).

Fig. 9 shows an example of W-band compression waveforms in a dual target measurement, with $\theta_1 = 1.4°$ and $\theta_2 = -0.5°$. The return signals from the two targets are clearly resolved. The expanded views in Figs. 9(b,c) illustrate that the lead-lag phase relationship between Σ- and Δ-mode compression peaks is reversed for Target 1 compared to Target 2, as expected due to the different signs of the target angles. In our processing procedure, the cross-correlations are time-windowed to select the signal from an individual target. As before, we then use Eq. (16) to obtain $|\theta|$, and we compute the cross-correlation between Σ- and Δ-mode compression traces to return the sign of θ for the selected target. This procedure is then repeated for the other target.

The retrieved angles of Targets 1 and 2 are plotted in Figs. 8(b) and 8(c) as Target 1 is scanned in angle, for range differences of 4.7 cm and 2.5 cm, respectively, between the two targets. In both the figures, the angle of the stationary target (Target 2) is approximately constant ($\theta_2 \approx -0.5°$ in Fig. 8(b) and $\theta_2 \approx -0.4°$ in Fig. 8(c)), as expected. The retrieved angles of the moving target (Target 1) predominantly follow a linear relation in the intended actual target angle with slope one. At small target angles, $|\theta| < 0.4°$, the sensing accuracy is observed to degrade, similar to what was observed in the single target experiments. The low amplitude of the Δ-mode waveforms near $\theta = 0°$ increases susceptibility to noise, which leads to larger errors in the angle estimate see Eq. (16). The finite aperture of the targets may also play a role (both for dual-target as well as single target experiments). Each target subtends an arc of $2°$ when placed at a range of 3 m, which can also lead to incomplete extinction of the Δ-mode signal. To a lesser extent, the accuracy of the retrieved angles also appears to degrade when the moving target gets close to $\pm4°$. This observation is likely related to the angular response of the individual antennas, which falls off beyond roughly $\pm2°$, see Fig. 5(e), as well as to the array factor for Σ-mode transmission, which has a zero near $\pm4°$, see Fig. 3(d). Both effects reduce signal-to-noise. Finally, in the dual target measurements, cross-correlation sidelobes are also an issue. As the difference in ranges becomes small, sidelobes from the cross-correlation of one target begin to overlap with the peak of the other; such crosstalk degrades accuracy for angular as well as range sensing. Even so, the respective RMS errors in
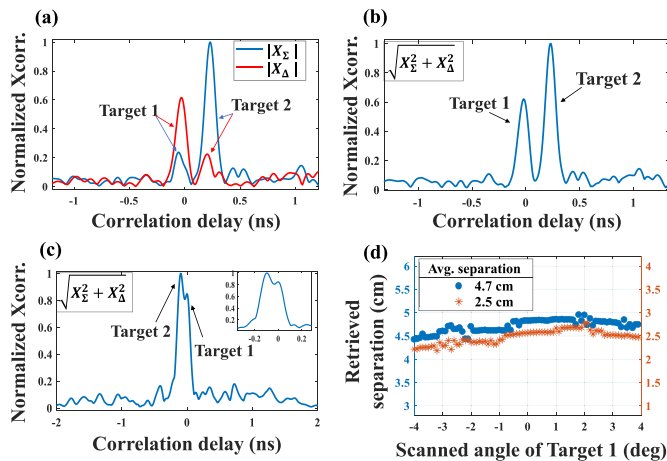
Fig. 10. (a) Examples of Σ- and Δ-mode W-band compression trace absolute-valued envelopes (envelopes of $|X_\Sigma|$ and $|X_\Delta|$) when the targets are separated by 4.7 cm, with angular shift of target 1 and target 2 being -3.7^o and -0.5^o respectively. (b) Envelope of root-mean-square trace obtained from compression traces in (a). (c) Example of root-mean-square trace envelope obtained from X_Σ and X_Δ at target spacing of 1.5 cm. (d) Retrieved target spacing (for two settings) as a function of angular displacement of the moving target.

the retrieved angles of Target 1 and Target 2 are only 0.44^o and 0.06^o for a target separation of 4.7 cm; the RMS errors for a target separation of 2.5 cm are 0.97^o and 0.24^o, respectively.

2) Range Estimation: The difference in the ranges of two targets (Δr) can be identified from the temporal separation of their respective compression peaks (Δt) via $\Delta t = 2\frac{\Delta r}{c}$. Fig. 10(a) shows representative dual target results for $\Delta r = 4.7$ cm. Here we plot the envelopes of Σ- and Δ-mode compression waveforms, obtained by interpolating the maxima of the carrier oscillations in the W-band compression waveforms and taking the absolute value. As we have seen before, the relative amplitudes of Σ- and Δ-mode waveforms depends strongly on target angle. Therefore, we compute the root-mean-square trace $\sqrt{(X_\Sigma^2 + X_\Delta^2)}$, where here X_Σ and X_Δ respectively refer to the envelopes of the Σ- and Δ-mode compression waveforms. Fig. 10(b) shows the root-mean-square trace corresponding to the compression waveforms in Fig. 10(a). The two targets are clearly resolved, and the remaining difference in the amplitudes of the two peaks is largely due to the angular response function of the antennae. Fig. 10(c) shows similar data for $\Delta r = 1.5$ cm, which illustrates the minimum range resolution achieved in these experiments. The two correlation peaks are just barely distinguished. Their separation Δt is 100 ps, comparable the full-width at half maximum (FWHM $\sim$110 ps) of the peak from a single target. However, when the range difference is this small, angular sensing is compromised due to excessive waveform overlap. For the waveforms used in our experiments, we find that a minimum range difference of $\sim$2.5 cm is required for independent angular sensing of the dual targets.

Retrieved range differences (Δr) are shown in Fig. 10(d) as the angle of Target 1 is varied with Target 2 fixed. The experiment was repeated for average range differences of 4.7 cm and 2.5 cm. The intent of this experiment is to determine the error bar in measured range. However, nonidealities in the mechanical

angular scan of Target 1 can lead to a weak variation of its range with angle. Since this variation should not depend on the range itself, the difference in the measured Δr should then be independent of angle. This trend is evident in Fig. 10(d). Therefore, by computing the variation in the range difference with angle, we obtain a better estimate of the uncertainty in the range measurement. In this way we assess a 0.4 mm RMS uncertainty in the range measurement.

V. DISCUSSION AND CONCLUSION

In summary, we have demonstrated two-dimensional radar imaging using photonically generated, broadband waveforms in the RF W-band. The broad bandwidth (spectral content from 80-95 GHz at -10 dB) enables range measurements with $\sim$1.5 cm resolution and sub-mm error, while the ability to generate independent broadband waveforms feeding a two element transmit array permits measurement of azimuthal angle. Our approach is analogous to monopulse radar, which obtains target angle information through joint processing of sum and difference patterns using beamforming networks following simple receive antenna arrays; however, in our work the sum and difference patterns are achieved at the transmitter side by exciting the array with in-phase and out-of-phase broadband waveforms. Our experiments take advantage of the unique ability of photonics-based generation to impose uniform phase shifts and control far-field interference across the entire bandwidth of interest. Our technique is applicable either for range and azimuth sensing of a single target or for sensing of multiple targets, provided that the targets are resolved in range. The current experiments demonstrate simultaneous sensing of the range difference and the individual angles of two targets.

There are several ways to extend or improve beyond the current proof-of-concept experiments. For example, sharper compression peaks can be obtained by increasing the bandwidth, as in previous experiments with a single transmit antenna that used chirp waveforms spanning the full W-band (75-110 GHz) [2]. Furthermore, more careful spectral engineering [36] to obtain smoother or apodized spectral envelopes would reduce cross-correlation sidelobes. Both of these would permit resolution of targets at smaller range difference, necessary for simultaneous acquisition of independent target angles. Another enhancement could entail application of an expanded set of phase shifted waveforms, e.g., waveforms with broadband phase shifts of 0, $\pm\pi/2$, and π as opposed to waveforms with just 0 and π phase shifts used currently. Generation of families of broadband RF waveforms subject to quadrature or even higher order phase shift keying has been demonstrated by related photonics-based generation techniques [24]. The use of an expanded number of phase shifts could be particularly helpful in reducing angular measurement uncertainties along directions where either the Σ-mode or Δ-mode signal is zero and hence sensitive to noise and cross-correlation sidelobes. The ability to photonically switch between waveforms with different broadband RF phase shifts at hundreds of MHz rates has also been demonstrated [24] and could contribute to faster detection methods. Rapid modulation or switching of waveforms can also increase

the window over which range can be unambiguously measured. In the current setup the unambiguous measurement window is limited by the 4 ns repetition period of the mode-locked laser. However, as demonstrated in our group's previous single antenna work [2], [37], the waveform repetition period can be expanded by switching the polarity of the transmitted broadband waveforms on a pulse by pulse basis according to a predefined pseudorandom sequence. This approach can be generalized to multiple transmit antennas. By adjusting the length of the pseudorandom sequence, the unambiguous detection window can in principle be made arbitrarily large. Finally, one can use lower gain antennas for a larger field of view, as well as potentially increase the number of transmit antennas (each of which will be driven by an independently controllable, photonically generated RF waveform). A particularly interesting case would comprise four transmit antennas in a square array for Σ- and Δ-mode operation in both horizontal and vertical directions, enabling three-dimensional imaging.

REFERENCES

[1] T.-F. Tseng, J.-M. Wun, W. Chen, S.-W. Peng, J.-W. Shi, and C.-K. Sun, "High-depth-resolution 3-Dimensional radar-imaging system based on a few-cycle W-band photonic millimeter-wave pulse generator," *Opt. Express*, vol. 21, no. 12, pp. 14 109–14 119, 2013.

[2] Y. Li, A. Rashidinejad, J.-M. Wun, D. E. Leaird, J.-W. Shi, and A. M. Weiner, "Photonic generation of W-band arbitrary waveforms with high time-bandwidth products enabling 3.9 mm range resolution," *Optica*, vol. 1, no. 6, pp. 446–454, 2014.

[3] J. Federici and L. Moeller, "Review of terahertz and subterahertz wireless communications," *J. Appl. Phys.*, vol. 107, no. 11, p. 6, 2010.

[4] J.-W. Shi, C.-B. Huang, and C.-L. Pan, "Millimeter-wave photonic wireless links for very high data rate communication," *NPG Asia Mater.*, vol. 3, no. 4, pp. 41–48, Apr. 2011.

[5] N.-W. Chen et al., "Design and demonstration of ultra-fast W-band photonic transmitter-mixer and detectors for 25 Gbits/sec error-free wireless linking," *Opt. Express*, vol. 20, no. 19, pp. 21 223–21 234, 2012.

[6] S. Koenig et al., "Wireless sub-THz communication system with high data rate," *Nature Photon.*, vol. 7, no. 12, pp. 977–981, Oct. 2013.

[7] T. Nagatsuma et al., "Terahertz wireless communications based on photonics technologies," *Opt. Express*, vol. 21, no. 20, pp. 23 736–23 747, 2013.

[8] S. Saponara, F. Giannetti, B. Neri, and G. Anastasi, "Exploiting mm-wave communications to boost the performance of industrial wireless networks," *IEEE Trans. Ind. Inform.*, vol. 13, no. 3, pp. 1460–1470, Jun. 2017.

[9] R. McMillan, "Terahertz imaging, millimeter-wave radar," in *Proc. Adv. Sensing Security Appl.*, Berlin, Germany, 2006, pp. 243–268.

[10] M. Tonouchi, "Cutting-edge terahertz technology," *Nature Photon.*, vol. 1, no. 2, pp. 97–105, 2007.

[11] R. Appleby and R. N. Anderton, "Millimeter-wave and submillimeter-wave imaging for security and surveillance," *Proc. IEEE*, vol. 95, no. 8, pp. 1683–1690, Aug. 2007.

[12] M. Kishida, K. Ohguchi, and M. Shono, "79 GHz-band high-resolution millimeter-wave radar," *Fujitsu Sci. Tech. J*, vol. 51, no. 4, pp. 55–59, 2015.

[13] P. Molchanov, S. Gupta, K. Kim, and K. Pulli, "Short-range FMCW monopulse radar for hand-gesture sensing," in *Proc. IEEE Radar Conf. (RadarCon)*. 2015, pp. 1491–1496.

[14] K. B. Cooper et al., "Penetrating 3-D imaging at 4- and 25-m range using a submillimeter-wave radar," *IEEE Trans. Microw. Theory Techn.*, vol. 56, no. 12, pp. 2771–2778, Dec. 2008.

[15] J. Yao, "Microwave photonics," *J. Lightw. Technol.*, vol. 27, no. 3, pp. 314–335, 2009.

[16] P. Ghelfi et al., "A fully photonics-based coherent radar system," *Nature*, vol. 507, pp. 341–345, Apr. 2014.

[17] R. Rotman, M. Tur, and L. Yaron, "True time delay in phased arrays," *Proc. IEEE*, vol. 104, no. 3, pp. 504–518, Mar. 2016.

[18] B. Gao, F. Zhang, E. Zhao, D. Zhang, and S. Pan, "High-resolution phased array radar imaging by photonics-based broadband digital beamforming," *Opt. Express*, vol. 27, no. 9, pp. 13 194–13 203, 2019.

[19] A. Rashidinejad, Y. Li, and A. M. Weiner, "Recent advances in programmable photonic-assisted ultrabroadband radio-frequency arbitrary waveform generation," *IEEE J. Quantum Electron.*, vol. 52, no. 1, pp. 1–17, Jan. 2016.

[20] A. M. Weiner, "Femtosecond pulse shaping using spatial light modulators," *Rev. Sci. Instrum.*, vol. 71, no. 5, pp. 1929–1960, 2000.

[21] A. Dezfooliyan and A. M. Weiner, "Photonic synthesis of high fidelity microwave arbitrary waveforms using near field frequency to time mapping," *Opt. Express*, vol. 21, no. 19, pp. 22 974–22 987, 2013.

[22] J. Chou, Y. Han, and B. Jalali, "Adaptive RF-photonic arbitrary waveform generator," *IEEE Photon. Technol. Lett.*, vol. 15, no. 4, pp. 581–583, Apr. 2003.

[23] I. S. Lin, J. D. McKinney, and A. M. Weiner, "Photonic synthesis of broadband microwave arbitrary waveforms applicable to ultra-wideband communication," *IEEE Microw. Wireless Compon. Lett.*, vol. 15, no. 4, pp. 226–228, 2005.

[24] A. Rashidinejad, D. E. Leaird, and A. M. Weiner, "Ultrabroadband radio-frequency arbitrary waveform generation with high-speed phase and amplitude modulation capability," *Opt. Express*, vol. 23, no. 9, pp. 12 265–12 273, 2015.

[25] N.-W. Chen, H.-J. Tsai, F.-M. Kuo, and J.-W. Shi, "High-speed W-band integrated photonic transmitter for radio-over-fiber applications," *IEEE Trans. Microw. Theory Techn.*, vol. 59, no. 4, pp. 978–986, Apr. 2011.

[26] S. Wang, K.-H. Tsai, K.-K. Huang, S.-X. Li, H.-S. Wu, and C.-K. C. Tzuang, "Design of X-band RF CMOS transceiver for FMCW monopulse radar," *IEEE Trans. Microw. Theory Techn.*, vol. 57, no. 1, pp. 61–70, Jan. 2009.

[27] M. I. Skolnik, *Radar handbook second edition*, New York, NY, USA: McGrawHill, 1990.

[28] S. M. Sherman and D. K. Barton, *Monopulse Principles and Techniques*. Norwood, MA, USA: Artech House, 2011.

[29] S. Preussler, F. Schwartau, J. Schoebel, and T. Schneider, "Photonically synchronized large aperture radar for autonomous driving," *Opt. Express*, vol. 27, no. 2, pp. 1199–1207, Jan. 2019.

[30] A. Kanno and T. Kawanishi, "Broadband frequency-modulated continuous-wave signal generation by optical modulation technique," *J. Lightw. Technol.*, vol. 32, no. 20, pp. 3566–3572, 2014.

[31] T. Kawanishi, A. Kanno, P. Tien Dat, T. Umezawa, and N. Yamamoto, "Photonic systems and devices for linear cell radar," *Appl. Sci.*, vol. 9, no. 3, 2019, Art. no. 554.

[32] M. Ruegg, E. Meier, and D. Nuesch, "Capabilities of dual-frequency millimeter wave SAR with monopulse processing for ground moving target indication," *IEEE Trans. Geosci. Remote Sensing*, vol. 45, no. 3, pp. 539–553, Mar. 2007.

[33] B. Liu et al., "Extremely wide bandwidth microwave photonic phase shifter for W-band chirped monopulse radar," in *Proc. Opt. Fiber Commun. Conf.*, 2018, pp. 1–3.

[34] B. Liu et al., "Ultra-broadband photonic monopulse-like radar for remote sensing," in *Proc. CLEO: Appl. Technol.*, 2019, pp. 1–2.

[35] N. Levanon, *Radar Principles* New York, NY, USA: Wiley, p. 320, May 1988.

[36] J. D. McKinney, I. S. Lin, and A. M. Weiner, "Shaping the power spectrum of ultra-wideband radio-frequency signals," *IEEE Trans. Microw. Theory Techn.*, vol. 54, no. 12, pp. 4247–4255, Dec. 2006.

[37] Y. Li, A. Dezfooliyan, and A. M. Weiner, "Photonic synthesis of spread spectrum radio frequency waveforms with arbitrarily long time apertures," *J. Lightw. Technol.*, vol. 32, no. 20, pp. 3580–3587, Oct. 2014.